**ASSESSMENT OF ANORTHOSITE ON THE MOON USING LROC NARROW ANGLE CAMERA PHOTOMETRY: CORRELATIONS BETWEEN SINGLE SCATTERING ALBEDO, COMPOSITION, AND OPTICAL MATURITY.**

B. L. Jolliff[1], A. R. Schonwald[1], and R. N. Watkins[2], [1]Department of Earth and Planetary Sciences and the McDonnell Center for the Space Sciences, Washington University in St. Louis, Campus Box 1169, 1 Brookings Drive, Saint Louis, MO 63130, USA, [2] Planetary Science Institute, 1700 E. Fort Lowell, Suite 106, Tucson, AZ 85719, USA. (bjolliff@wustl.edu)

**Introduction:** Lunar orbital datasets with high spatial and spectral resolution have led to the identification of very pure anorthosite (i.e., >98% plagioclase) at numerous locations [1-3]. Such identifications use the 1250 nm ferrous absorption caused by minor amounts of FeO in plagioclase [1,4]. These identifications, which are detected in central peaks of complex craters and uplift structures of impact basins have been interpreted to reflect a highly anorthositic crustal layer beneath the megaregolith and perhaps extending to the base of the primary crust [1]. This interpretation has great significance for both the $Al_2O_3$ content and lithologic makeup of the lunar crust and upper mantle [5], and for the mechanism of plagioclase enrichment in the crust, presumably related to magma ocean differentiation [e.g., 6-8].

In this abstract, we explore relationships between photometric parameters at very high spatial resolution, with data obtained by the Lunar Reconnaissance Orbiter Camera (LROC) Narrow Angle Camera (NAC), and the occurrence of anorthosite based on hyperspectral reflectance data ($M^3$, Kaguya spectral suite). We also explore the relationship between the photometric data and optical maturity. We focus on the single scattering albedo, SSA or *w*, and the local distribution of anorthosite in locations of "purest anorthosite" or PAN [1-3] detection.

**Methods and Data:** In this work, we follow methods outlined in [9]. We use USGS Integrated Software for Imagers and Spectrometers (ISIS3) to process LROC NAC images for locations where we also have NAC Digital Topographic Model (DTM) data. We resample NAC image data to NAC DTM resolution (~5 mpp), and we then use the specific illumination geometry of each image to calculate the incidence and emission angle for every pixel in the scene [10]. The local illumination geometry is then used in the Hapke equation [11,12] to calculate the single-scattering albedo (SSA). We make simplifying assumptions about parameters (e.g., grain size, space-weathering maturity) and calculate SSA (*w*) using a two-parameter optimization algorithm [13,14].

For this work, we have investigated two sites along the Inner Rook Ring (IRR) massifs of Orientale basin, one on the eastern side (IRR1: 273.434°E and 19.527°S) and one on the northern side (IRR2: 264.10°E, 11.08°S); the central peak of Korolev-M crater (202.70°E, 8.50°S); and the northern rim of Hertzsprung basin (229.60°E, 5.16°N). We use LROC NAC images and corresponding DTMs for each of these sites, along with Kaguya-derived optical maturity (OMAT) data [16] and Clementine FeO. We use Moon Mineralogy Mapper ($M^3$) data [17] with the ground-truth correction applied to Level 2 and the continuum removal tool in ENVI version 5.5 to better identify weak spectral absorptions.

**Results:** As shown by [10], we find a first-order correlation between the LROC-NAC-derived SSA and composition, illustrated here with FeO (Fig. 1) as representing mafic mineralogy. The correlation is related to the relative proportions of low-albedo mafic minerals and higher-albedo anorthosite. The correlation line established using Apollo soils projects, at the low FeO end, to anorthosite as seen at the IRR1 location at a *w*

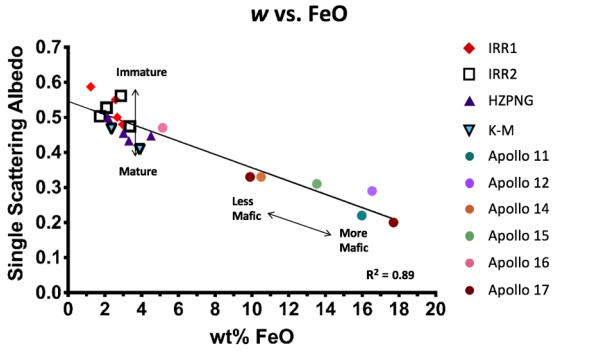


**Figure 1.** Relationship between SSA and FeO established for Apollo landing site soils [10] and PAN location soils [9]. Scatter above and below the correlation line is in large part a function of maturity whereas location along the line is largely a function of FeO content or mafic mineralogy.

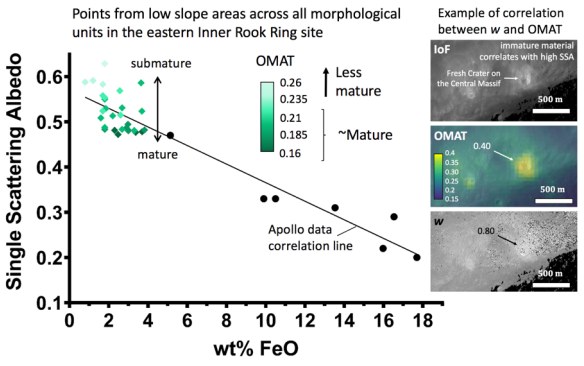


**Figure 2.** Illustration of the effect of soil maturity as measured by Kaguya OMAT [16] on SSA (*w*) from the IRR1 site. Scene on right is from north-facing slope of one of the massifs uplifted by the Orientale basin-forming impact.

value of ~0.55 and FeO<1 wt.% (Fig. 1). However, maturity also has a strong effect because freshly exposed material that has not been subjected long to space weathering has an apparent high albedo. This effect is illustrated by a small, fresh, highly reflective impact crater on the massif slope at IRR1 where the the OMAT value is 0.4 (immature) and the computed *w* value is 0.8 (Fig. 2).

In addition to fresh craters, slopes and on-going mass wasting also contribute to variations in maturity and thus in our computed *w* values. We illustrate this effect in Fig. 3, with the result that (1) we must take slopes into account even though we have used NAC-derived DTMs to determine the local illumination geometry for our photometric model. Small scale variations in the regolith surface fabric still cause variations in computed *w* values. (2) To minimize variations caused by differences in regolith maturity, we must compare areas with equal maturity, normalize the *w* data according to OMAT, or restrict comparisons to areas with mature regolith.

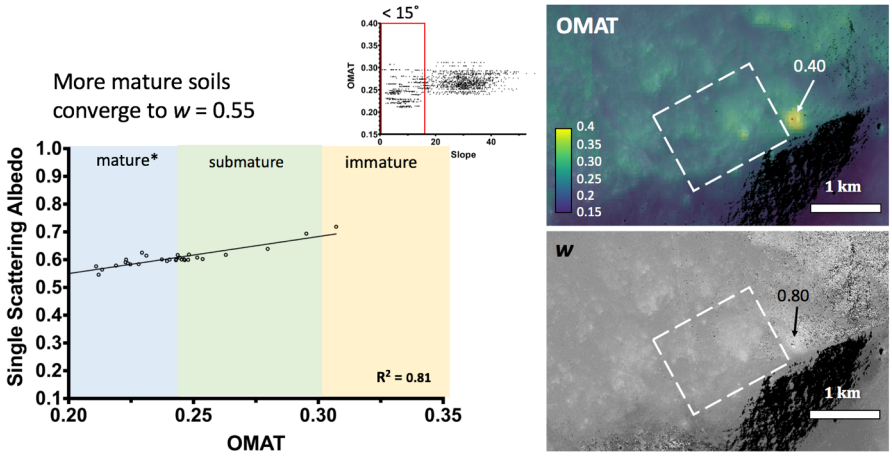


**Figure 3.** Variation of SSA (*w*) with surface maturity (OMAT) in an area with slopes. Data from a polygon on a massif at IRR1 comparing *w* and OMAT (right side). Inset at top shows variation of OMAT with slope; multiple slope values are plotted per OMAT value owing to the differing resolution of the datasets. Restricting the data to less than 15 degree slopes and convolving *w* to OMAT resolution yields the plot of SSA vs OMAT. *Maturity categorization comes from correlation between OMAT and $I_S$/FeO [18].

**Discussion:** Our objective is to be able to map variations in SSA at NAC resolution (or, at least with NAC DTM-scale resolution of ~5 mpp) to assess local variations in regolith composition and thus the dominant rock types that contribute to or make up the regolith. At issue is the distribution and purity of anorthosite. "Purest anorthosite" or PAN is defined to have >98% plagioclase, which is a difficult purity to obtain by igneous cumulate processes because trapped melt must be removed from interstices with almost 100% efficiency. Although this may occur on hand-sample scale, it is far less likely to occur on scales of kilometers or to dominate large portions of the middle and lower crust.

With all of the caveats discussed above, and taking into account variations in slope, maturity, and illumination geometry, and our best assessment of how SSA varies with FeO, we find that the sites we have investigated exhibit regolith FeO contents consistent with anorthosite (>90% plagioclase) but not "purest anorthosite (>98% plagioclase) and rarely >95% (Fig. 4).

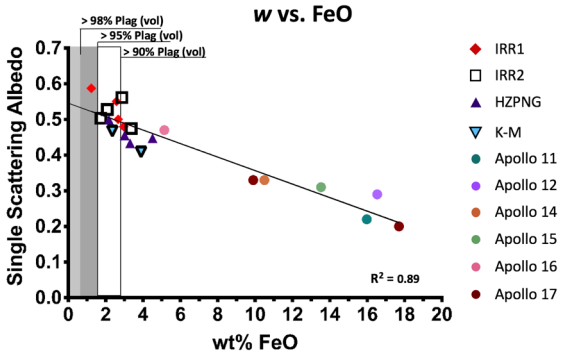


**Figure 4.** Plagioclase contents corresponding to low FeO contents for morphologic units at the study sites.

**Conclusions:** Regolith compositions that we infer from SSA variations reflect contributions from source rocks more mafic than PAN at the study sites. The implication is that on average the source rocks are more mafic or include more mafic middle- to lower-crustal rocks, also concluded by [5].

**Acknowledgments:** Thanks to NASA for support of the LRO extended mission and for the hard work of the LRO and LROC Operations Teams. We appreciate colleagues at ASU for production of NAC DTMs.

**References:** [1] Ohtake M. et al. (2009) *Nature* **461**, 236-241. [2] Cheek L. et al. (2013) *JGR*, **118**, 1805-1820. [3] Donaldson-Hanna K. et al. (2014) *JGR*, **119**, 1516-1545. [4] Cheek L. & Pieters C. (2014) *Amer. Mineral.* **99**, 1871-1892. [5] Lemelin M. et al. (2019) *PSS* **165**, 230-243. [6] Longhi J. (2003) *JGR* **108**, 5083. [7] Elardo S. (2011) *GCA* **75**, 3024-3045. [8] Charlier B. et al. (2018) *GCA* **234**, 50-69. [9] Schonwald A. et al. (2019) *LPSC* **50**, #1239. [10] Clegg-Watkins, R. et al. (2017) *Icarus* **285**, 169-184. [11] Hapke B. (2012a) *Icarus*, **221** (2), 1079-1083. [12] Hapke B. (2012b) *Theory of Reflectance and Emittance Spectroscopy* (2nd Ed.). [13] Hahn T. et al. (2018) *LPSC* **49**. #2637. [15] Hahn T. et al. (2019) *LPSC* **50**. #1976. [16] Lemelin M. (2016) *LPSC* **47**, #2994. [17] Pieters C. et al. (2009) *Current Science* **96** (4), 500-505. [18] Lucey P. et al. (2000) *JGR* **105**, 20377-20386.